A Neuromorphic aVLSI Model of Global Motion Processing in the Fly

Shih-Chii Liu

***Abstract*—Flies orientate themselves quickly in an unstructured environment through motion information computed from their low-resolution compound eyes. The fly visual system is an example of a robust motion system that works in a natural environment. In this paper, we describe a low-power analog very large scale integration chip that models motion computation in the fly. The architecture of this motion chip closely follows the anatomical layout of of the fly visual layers. The output of the chip corresponds to the responses of the wide-field direction-selective cells in the final layer of the visual system. The silicon chip has a one-dimensional array of 37 elementary motion detectors (EMDs) each of which provides local motion information. The EMD outputs are aggregated in a nonlinear way to produce a motion output that is independent of the stimulus size and contrast. We employed various circuit techniques to ensure robust motion computation in each processing stage. Results from the circuit fabricated in a 1.2-μm CMOS technology are compared with the responses of the direction-selective cells.**

***Index Terms*—analog integrated circuits, biological cells, biological system modeling, motion analysis, neural network hardware, very-large-scale integration.**

I. Introduction

CONVENTIONAL motion sensors usually work well only under predefined conditions. Computer vision techniques use serially-scanned high-resolution charge coupled device (CCD) imagers and frame-based processing, and require a fast computational engine. Neuromorphic chips offer a variety of low-power, single-chip solutions for computing the motion of stimuli with a wide range of contrasts and speeds, under a large dynamic range of lighting conditions [1], [2], [9], [5], [12], [17], [21], [23], [24]. These solutions are based on algorithms that model the motion computation in biological systems.

In this work, we describe a low-power, analog very-large-scale-integrated (aVLSI) motion sensor that models the motion computation believed to be performed in the fly visual system [14]. We use the fly visual system as our model since flies are capable of navigating rapidly in an unstructured environment with low-resolution visual information. The resolution of their compound eyes approximates that of a low-resolution 60×60 pixel imager. By modeling the motion system of the fly on silicon and ultimately mounting these motion sensors on a robotic platform, we can also investigate continuous-time visual-guided behaviors on a robot without being hampered by CCD imagers that require a high scanout rate for real-time interaction.

The architecture of this chip closely follows the anatomical layout of the processing layers in the fly visual system. The details of the anatomy and physiology of the fly visual system is described in Section II. The global motion output is generated from the nonlinear aggregation of 37 elementary motion detectors (EMDs). The circuits of the different layers in the architecture are described in Sections III and IV. We employed different circuit techniques to reduce the effects of background intensity and mismatches between layers of processing within each pixel. These techniques are described in Section V. Measured results from a chip fabricated in a 1.2-μm CMOS technology are presented in Sections VI and VII. We compare the chip results with the responses of the wide-field direction-selective cells in the fly.

II. Biological Background

Each of the two compound eyes of the fly consists of 3000–4000 ommatidia (or "little eyes"), each with its own lens. The compound eye has a resolution of about 1.5° and is equivalent to a 60×60 imager (depending on the species). Thus, the fly does not need high spatial resolution information to compute optical flow information needed for navigation. The visual system of the fly consists of four layers: the retina, the lamina, the medulla, and the lobula complex. The retinotopic arrangement of the pixels in the first three layers of the visual system makes it easy to map the structure of the system to silicon.

The photoreceptors in the retina transduce the incoming light into a voltage signal. Each photoreceptor employs local gain control by adapting to the background intensity, thus ensuring that the receptor has a high transient gain to changes in intensity and a low dc gain. The receptor primarily codes contrast information. The laminar monopolar cells (LMCs) perform a temporal bandpass filtering of the receptor signals without retaining any information about the background intensity [16], [18]. The LMC output is an amplified and inverted version of the receptor signal. Very little is known about the functionality of the cells in the medulla since the small size of the cells make them difficult to record.

There are 50–60 wide-field direction-selective cells in the lobula plate. Most of them respond to moving stimuli with graded responses. The remaining cells in the lobula plate respond with spikes. The outputs of all the direction-selective cells provide information about the translational motion along and rotational motion about different axes in the visual field.

Manuscript received October 1999; revised August 2000. This work was supported in part under a Swiss National Foundation Research SPP Grant and in part by the Office of Naval Research. This paper was recommended by Associate Editor T. S. Lande.

The author is with the Institute of Neuroinformatics, CH-8057 Zurich, Switzerland.

Publisher Item Identifier S 1057-7130(00)11031-6.

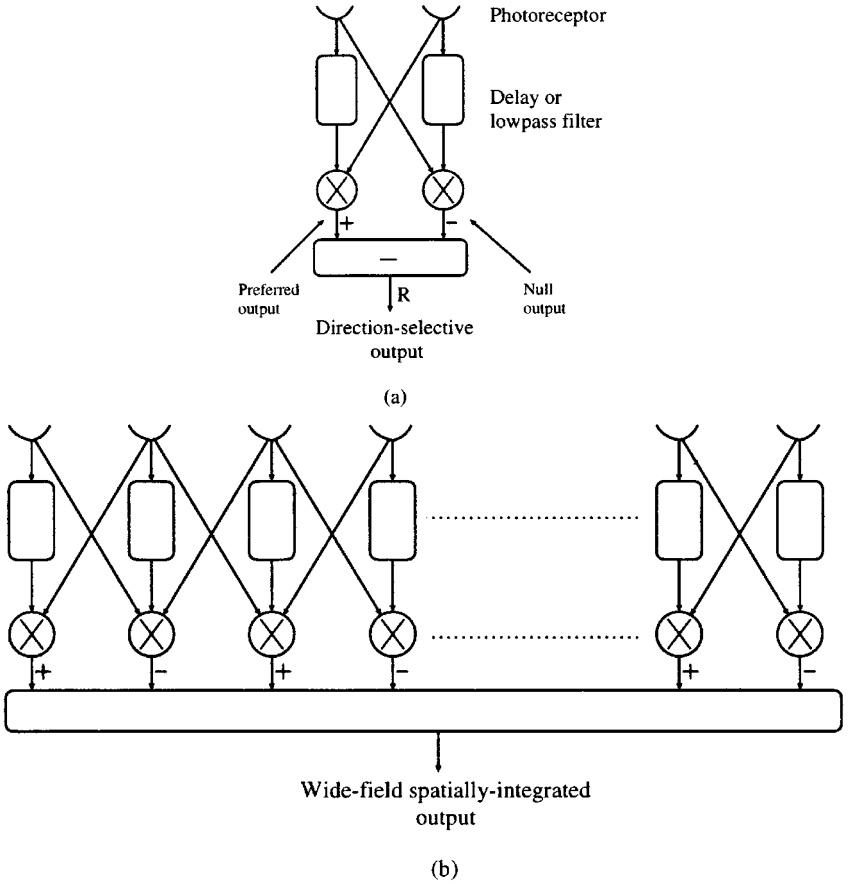

Fig. 1. Block diagram of Hassenstein–Reichardt's correlation model of motion computation in insects. (a) Model of a single EMD. (b) Model of a wide-field cell. Output is integrated from all EMDs. This is also the model of the motion sensor in this work.

This information controls the fly's motor reflexes during flight. The responses of these cells can be modeled by the spatial integration of the outputs of local (EMDs). The first EMD model, Fig. 1(a), was first proposed by Hassenstein and Reichardt in 1956 [14] and the spatial integration of the outputs of the EMDs by a wide-field direction-selective cell is shown in Fig. 1(b). Hassenstein and Reichardt's model was based on the optomotor response of the weevil *Chlorophanus*, but it also reproduces the responses of the wide-field cells. An EMD receives inputs from two neighboring pixels (or photoreceptors). One of the inputs is delayed through a lowpass filter. This delayed signal is multiplied with the input at the adjacent pixel. The output of the left multiplier of the EMD is sensitive to stimuli moving from left to right, while the output of the right multiplier is sensitive to stimuli moving from right to left. The two outputs are subtracted to remove the common-mode or flicker dependence on the input.

To compute the EMD output, R in Fig. 1(a), we assume that the input to a receptor is a sine wave $I + \Delta I \sin(\omega t + \theta)$ and the input to the neighboring receptor is $I + \Delta I \sin(\omega t + \theta + (2\pi a/\lambda))$. Here I is the mean intensity level, ω is the temporal frequency, λ is the spatial wavelength, θ is the spatial phase of the sinewave, and a is the pixel spacing. The output R can then be expressed as

$$R = \Delta I^2 \frac{\omega\tau}{1+\omega^2\tau^2} \sin\left(\frac{2\pi a}{\lambda}\right) d \qquad (1)$$

where d is $+1$ for the preferred direction and is -1 for the null direction. Notice that the output is dependent on the input temporal frequency ω and the time constant τ of the lowpass filter. The dependence of R on the square of ΔI only holds true in the responses of the biological cells for contrasts below 0.3. For higher contrasts, the response saturates.

III. aVLSI Elementary Motion Detector

The architecture of one of the silicon EMDs is shown in Fig. 2. The circuitry comprising the layers in this architecture is described in this section. Unless otherwise mentioned, the circuits are operated in the subthreshold domain.

A. Photoreceptor

The adaptive photoreceptor circuit first described by Delbrück [6] and modified by Liu [19] in Fig. 3 transduces via a photodiode, the incoming light E into a voltage signal $V_{\rm ph}$. The output $V_{\rm ph}$ codes the logarithm of the light intensity E if M_5 is in subthreshold. Changes in the local intensity dE are amplified by the transient gain of the circuit A, which is determined by the ratio of the capacitors, that is, $A = (C_1 + C_2)/(C_1)$. The circuit adapts to the background intensity at a time constant that depends on the capacitors C_1 and C_2, and the conductance of the adaptive element M_1. The conductance of M_1 is set by its gate voltage V_b, which is derived from the source follower circuit on the right of Fig. 3. The details of the circuit are dis-

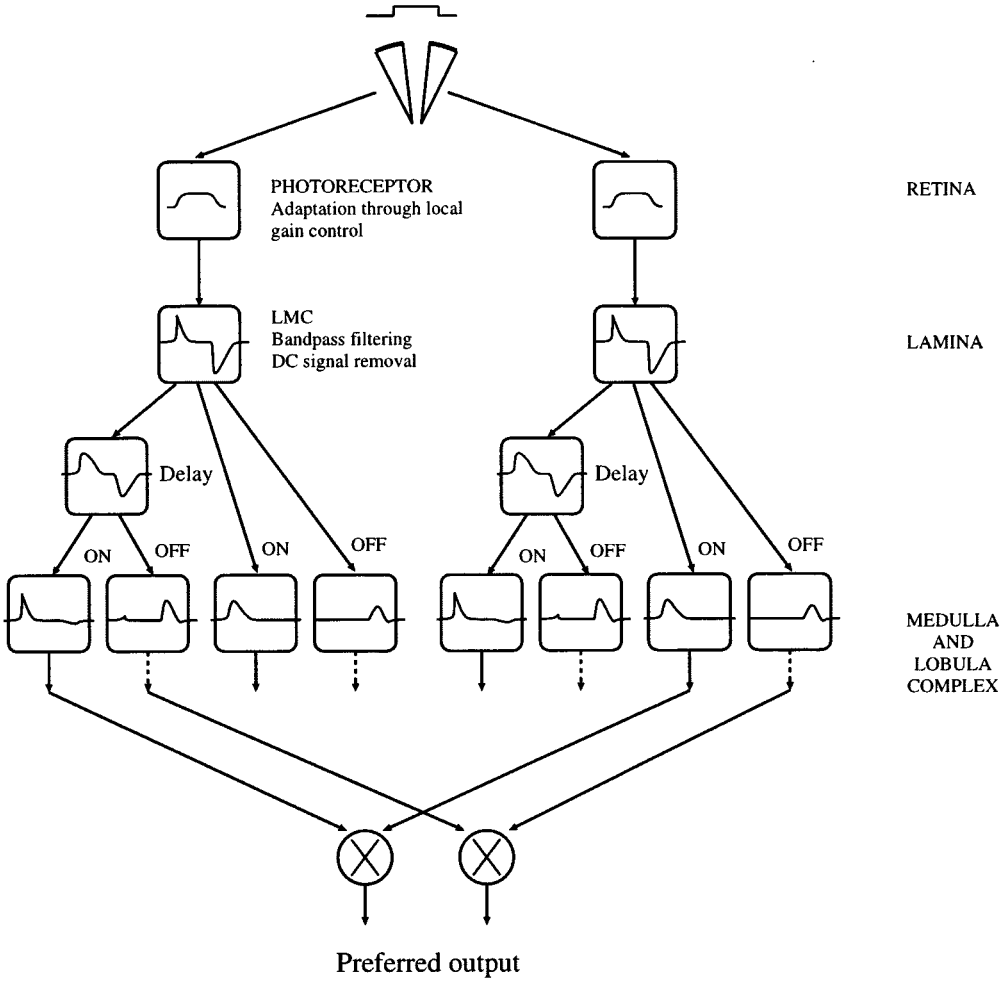

Fig. 2. Block diagram of the architecture of the silicon EMD for computing motion. The light input goes into a photoreceptor circuit with local gain control. The receptor output is then bandpass filtered by the LMC circuit. The output of the LMC circuit splits into two pathways. In one pathway, the signal is delayed through a low-pass filter. ON and OFF transient signals are generated from the delayed and undelayed signals. Subsequently, the ON and OFF delayed signals in each pixel are correlated (or multiplied) with the undelayed signals from the adjacent pixel. The two outputs in the figure are sensitive to a stimulus moving from left to right.

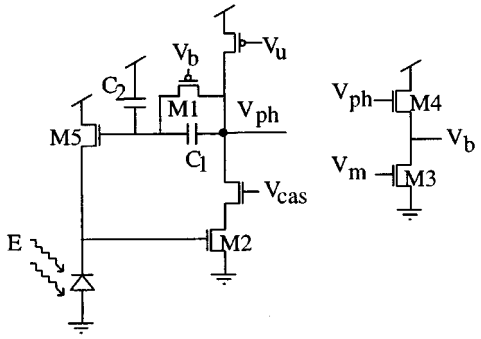

Fig. 3. Circuit diagram of photoreceptor circuit. The feedback consists of a resistor implemented by a pFET transistor M_1. The conductance of the resistor is controlled by the external bias V_m.

cussed in [19]. By changing the value of V_m, we can change the conductance of M_1. Hence, also the receptor's adaptation time constant. The transient change in $V_{\rm ph}$ in response to a step change in the intensity, (dE/E) can be described by

$$dV_{\rm ph} = U_T \frac{C_1 + C_2}{\kappa C_1} \frac{dE}{E} \tag{2}$$

where U_T is the thermal voltage and κ is the gate efficiency in driving the transistor. The output of the circuit responds primarily to the signal contrast and has a dc operating point that adapts to the background intensity.

B. Lamina

The circuitry in the second layer of the chip models the responses of the cells in the laminar layer. The response of the LMC cell is an amplified and inverted version of the input from the receptor. The dc dependence of the LMC output on the background intensity is zero. To implement this function, we use an inverting differentiator with an adaptive element M_9 between the output and the input as shown in Fig. 4(a). The transient gain in this circuit is set by the ratio of capacitors $(C_3 + C_4)/(C_4)$, i.e.,

$$\frac{dV_{\rm lmc}}{dV_{\rm ph}} = \frac{C_3 + C_4}{C_4}. \tag{3}$$

The output returns to its dc level that is set by the current in the bias transistor M_8. The time constant that the circuit takes to return to steady state is set by the capacitances and the conductance of M_9. The conductance of M_9 is set by a source follower

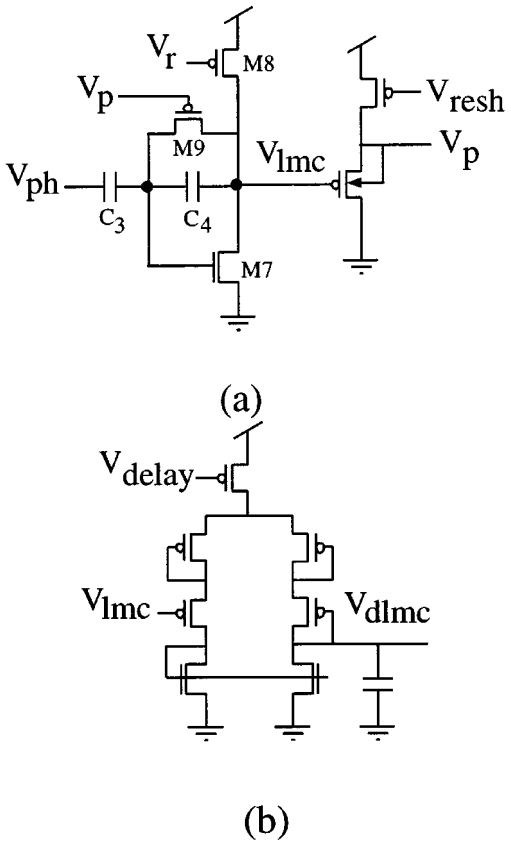

Fig. 4. Inverting differentiator and low-pass filter. (a) Inverting differentiator with active resistor implemented via a pass transistor M_9. The bias circuit that generates the bias voltage to M_9 is shown on the right. (b) Follower integrator used to implement the delay element with the input from $V_{\rm lmc}$. The linear range of the integrator was extended by using diode-connected transistors at the sources of the differential-pair input transistors.

circuit (as in the photoreceptor circuit). By highpass filtering the receptor output signal, we prevent dc mismatches in the photoreceptor output from affecting the operation of the LMC circuit. The step response of this circuit is shown in Fig. 5. The figure also shows how increasing $V_{\rm resh}$ decreases the conductance of the adaptive element M_9.

C. Low-Pass Filter

In the third layer of the chip architecture, we split the output of the LMC circuit into two pathways. In one pathway, the signal $V_{\rm lmc}$ is delayed through a low-pass filter. This filter is implemented by using a follower–integrator circuit [shown in Fig. 4(b)]. The follower circuit consists of a transconductance amplifier. Since the circuit is operated in subthreshold, the linear range of a normal five-transistor transconductance amplifier is limited to 100 mV. This limited input range causes the delayed output $V_{\rm dlmc}$ to slew-rate limit when the input signal changes by more than 100 mV, as it does with high contrast signals. The input range of the follower is extended by adding source-degeneration diodes in series with the input transistors of the transconductance amplifier to extend the linear range to about 300 mV.

D. Transient Current Generation

The fourth layer models possible properties of cells in the medulla and lobula complex of the fly visual system. Each pixel has two hysteretic differentiator circuits [17] (see Fig. 6), whose inputs come from $V_{\rm lmc}$ and $V_{\rm dlmc}$, respectively. In this circuit, we generate both an ON transient current $I_{\rm on}$ and an OFF transient current $I_{\rm off}$ from temporal changes in $V_{\rm lmc}$ and $V_{\rm dlmc}$. The currents $I_{\rm on}$ and $I_{\rm off}$ are given by

$$I_{\rm on} = C_5 \frac{dV_{fb}}{dt} \quad I_{\rm off} = -C_5 \frac{dV_{fb}}{dt}. \tag{4}$$

Only one current is on at a time, while the other is essentially zero. Using (2) and (3), and assuming that $(dV_{fb}/dt) = (dV_{\rm lmc}/dt)$, we get

$$I_{\rm on} = C_5 \frac{C_3 + C_4}{C_4} \frac{C_1 + C_2}{\kappa C_1} U_T \frac{1}{E} \frac{dE}{dt} \tag{5}$$

$$I_{\rm off} = -C_5 \frac{C_3 + C_4}{C_4} \frac{C_1 + C_2}{\kappa C_1} U_T \frac{1}{E} \frac{dE}{dt}. \tag{6}$$

The voltages $V_{\rm on1}$ and $V_{\rm off1}$ from the differentiator circuit in one pixel are correlated with the voltages $V_{\rm don2}$ and $V_{\rm doff2}$ from the differentiator circuit in the adjacent pixel using current correlators [4] (see Fig. 7). The current correlator, which is analogous to the multiplier in the Reichardt model, consists of two transistors in series. The output of the correlator consisting of M_1 and M_2 is

$$I_{\rm corr} = \frac{I_{\rm on1} I_{\rm don2}}{I_{\rm on1} + I_{\rm don2}}. \tag{7}$$

The currents from two of the correlators are summed together to create $I_{\rm pref}$, the output current for the preferred direction. The currents from the other two correlators are summed together to create $I_{\rm null}$, the output current for the null direction. These currents feed into the aggregating circuit, which is described in the following section.

IV. Nonlinear Integration of EMDs

The wide-field cells produce a global motion output from the aggregation of the outputs of the EMDs. A major concern in aggregating the outputs is that we have to ensure that the global motion measure is not confounded with the number of EMDS that are stimulated by the external environment. Images of the natural environment have roughly a $1/f$ distribution in their spatial power spectra with most of the power concentrated in the low spatial frequencies (that is, natural images have very few high contrast edges). Hence, many of the EMDs will not be stimulated when a fly is in a natural environment. If we simply sum the EMD outputs, then the motion output will increase as more EMDs are stimulated by the environment.

Both physiological recordings [11] and optomotor experiments [22] have shown that the outputs of the wide-field cells are independent of the stimulus size except for small-sized stimuli. This gain control property can be modeled by the biophysical properties of the cell and its dendrites as shown by Borst [3] (see Fig. 8). The membrane potential V_m of the cell is determined by the excitatory, inhibitory, and leak conductances g_e, g_i, and $g_{\rm leak}$, and the corresponding reversal potentials are E_e,

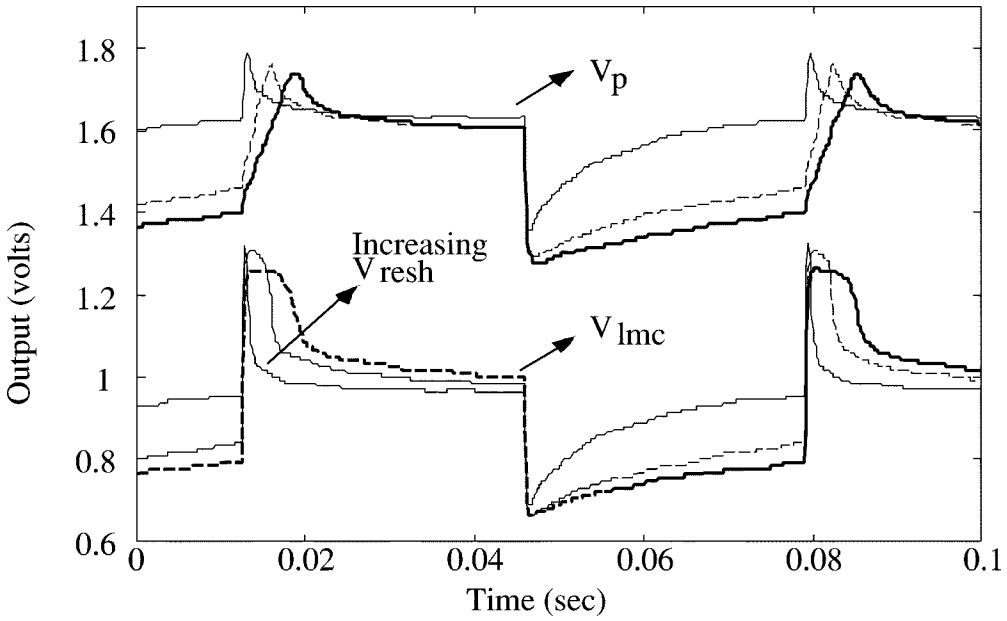

Fig. 5. Response of inverting differentiator to a 30-mV p–p square wave for different values of V_r and $V_{\rm rcsh}$. Response of $V_{\rm lmc}$ and V_p to different values of $V_{\rm rcsh}$.

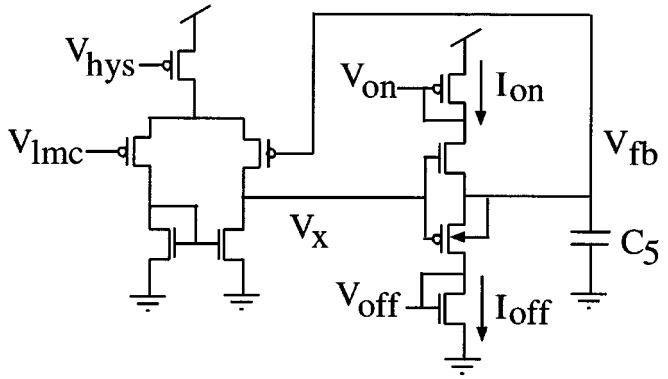

Fig. 6. Hysteretic differentiator circuit. This circuit generates transient currents $I_{\rm on}$ and $I_{\rm off}$ from changes in the output voltage $V_{\rm lmc}$, from the LMC circuit.

E_i, and $E_{\rm leak}$. The conductances g_e and g_i depend on the preferred and null motion outputs of an EMD, respectively. If the motion of the stimulus is in the preferred direction, then both g_e and g_i increase but $g_e > g_i$. The membrane potential can be written as

$$V_m = \frac{NE_e g_e + NE_i g_i + E_{\rm leak} g_{\rm leak}}{Ng_e + Ng_i + g_{\rm leak}} \tag{8}$$

where N is the number of activated EMDs. For large N and assuming $E_{\rm leak} = 0$, we get

$$V_m = E_e \frac{g_e - g_i}{g_e + g_i}. \tag{9}$$

In the equation above, we assume that $E_e = -E_i$. So for large N, the membrane potential only codes the motion independent of the number of activated EMDs.

We can map this model to the current-mode aggregator circuit shown in Fig. 9. Here, the outputs of the EMDs map to input currents (rather than conductances) and the reversal potential

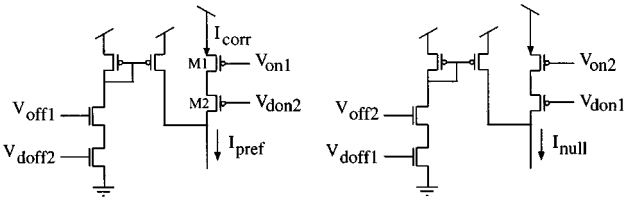

Fig. 7. Pairs of the output currents of the four current correlators are summed together to create $I_{\rm pref}$ and $I_{\rm null}$. Each correlator consists of two transistors in series, e.g., M_1 and M_2. The voltages $V_{\rm on1}$ and $V_{\rm off1}$ from the differentiator circuit in one pixel are correlated with the voltages $V_{\rm don2}$ and $V_{\rm doff2}$ from the differentiator circuit in the adjacent pixel.

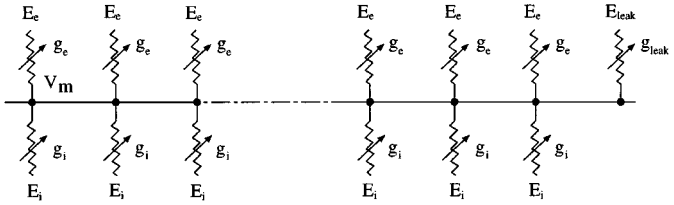

Fig. 8. Biophysical model of Borst [3] that models the aggregation property of wide-field cells. The membrane voltage V_m is determined by the excitatory, inhibitory, and leak conductances (g_e, g_i, and $g_{\rm leak}$) and their respective reversal potentials E_e, E_i, and $E_{\rm leak}$.

E_e sets the global bias current I_b. Each module consists of the transistors M_1 to M_7, which implement a Gilbert normalizer [10]. However, M_1, M_6, and M_7 are shared amongst all the modules so there are only four transistors in each module. The preferred $(I_{\rm pref})$ and null $(I_{\rm null})$ outputs of each silicon EMD are normalized with respect to the global bias current I_b. The input current $I_{\rm leak}$ acts as the leak conductance and determines the number of inputs at which the output saturates. The output current of the left leg $I_{\rm opref}$ of each module is given by

$$I_{\rm opref} = I_b \frac{I_{\rm pref}}{I_{\rm pref} + I_{\rm null} + I_{\rm leak}}. \tag{10}$$

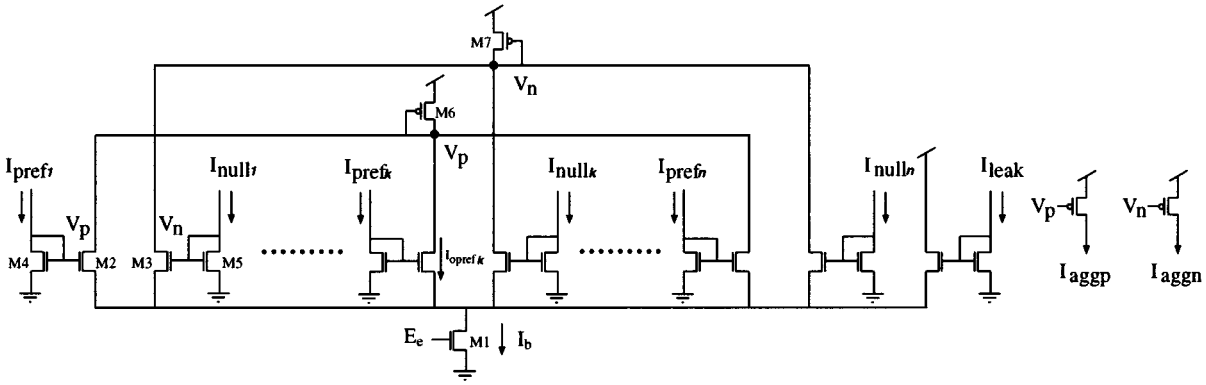

Fig. 9. Current-mode implementation of the aggregator model shown in Fig. 8. Each module of the aggregator circuit, represented by the transistors M_1 to M_7, implements a Gilbert normalizer circuit. The transistors M_1, M_6, and M_7 are shared amongst all the modules. The conductances in the biophysical model are represented by input currents $I_{\rm pref}$, $I_{\rm null}$, and $I_{\rm leak}$.

If N EMDs are activated and assuming that the preferred and null outputs are the same for all the N EMDs, then $I_{\rm opref}$ is now

$$I_{\rm opref} = I_b \frac{I_{\rm pref}}{NI_{\rm pref} + NI_{\rm null} + I_{\rm leak}}. \tag{11}$$

The global preferred current, $I_{\rm aggp}$, is the sum of all $I_{\rm opref}$s, i.e.,

$$\begin{aligned} I_{\rm aggp} &= \sum_{1}^{N} I_{\rm opref} \\ &= I_b \frac{NI_{\rm pref}}{NI_{\rm pref} + NI_{\rm null}} \\ &= I_b \frac{I_{\rm pref}}{I_{\rm pref} + I_{\rm null}} \end{aligned} \tag{12}$$

assuming that $NI_{\rm pref} + NI_{\rm null} \gg I_{\rm leak}$. Similarly, the global null current, $I_{\rm aggn}$ is given by

$$I_{\rm aggn} = I_b \frac{NI_{\rm null}}{NI_{\rm pref} + NI_{\rm null}} = I_b \frac{I_{\rm null}}{I_{\rm pref} + I_{\rm null}}. \tag{13}$$

We obtain the final motion output $I_{\rm mot}$ by subtracting $I_{\rm aggn}$ from $I_{\rm aggp}$, so

$$I_{\rm mot} = I_{\rm aggp} - I_{\rm aggn} = I_b \frac{I_{\rm pref} - I_{\rm null}}{I_{\rm pref} + I_{\rm null}}. \tag{14}$$

This equation is similar to the biophysical equation (9).

Harrison and Koch [13] recently demonstrated a voltage-mode implementation of the biophysical model in Fig. 8 where they used the preferred and null outputs of the EMD to control the bias currents of individual follower integrators. The inputs to the follower integrators come from E_e and E_i. The outputs of the integrators are shorted together. Since this implementation is in voltage mode, the authors have to ensure that the excitatory and inhibitory reversal potentials are close to each other so that the inputs to the followers V_m and one of the reversal potentials are within the limited input linear range of the followers. The current-mode implementation here does not suffer from the limited input linear range problem and uses only four transistors per module.

A nice property of spatially aggregating the outputs of the EMDs is that the temporal variation of the response of one EMD in response to a spatial grating input is removed in the final wide-field cell output. The reduction in the variation of the response occurs because the response of the EMDs to the moving pattern are spatially out of phase with each other. This phenomena has been demonstrated in the HS cell by Single, *et al.*using calcium imaging [25].

V. Mismatches

Silicon hardware, like biological neural hardware, has mismatches between pixels or cells on the same substrate. The coefficient of variation (CV)—defined as the standard deviation over the mean—of the mismatches from the biological LMC neurons is in the order of five percent between recorded cells [16]. The CV as measured from a silicon imager fabricated in a 2-μm CMOS ORBIT process is about 6%–10% [19]. The mean and standard deviation for the CV measure is obtained from the peak-to-peak responses of the photoreceptor output of the individual imager pixels in response to an LED that was modulated by a 10-Hz square wave. The pixels' mismatches need to be handled if comparisons or correlations between pixels are part of the motion computation algorithm.

We employed various circuit techniques to reduce the effects of mismatches and common-mode input factor in each processing stage. The ways we used to increase the robustness of the computation are as follows.

- We bandpass filtered the signal from the photoreceptor going into the LMC circuit so that there is no common-mode dependence on the LMC output.
- The dc level of the input from the LMC circuit to the hysteretic differentiator circuit affects the transient dynamics of the generation of the ON and OFF currents. Since the dc voltage of the LMC input to the hysteretic differentiator circuit is constant, the dynamics are not affected by the background light intensity.
- We have chosen to use transient current inputs instead of voltage inputs to a correlator circuit so that we would not have to deal with mismatches in the DC input levels at the multiplier. A previous hardware implementation of the correlation model, where voltage outputs from

neighboring pixels are fed into a multiplier circuit, failed to provide a robust direction-sensitive output. The signal was not robust because the input dc mismatches between the pixels creates different outputs at the multiplier. The use of transient currents ensures that there will be no output current (that is, zero motion signal) if there is no input change at the receptor output. The mismatches in the voltage multiplier could be reduced by layout and sizing techniques or nulled using tunnelling-injection structures [7] or UV techniques. Additional circuitry complexity and area would have been required to implement these features.

- We used current-mode circuits whenever possible (for example, in the nonlinear aggregator circuit) so that we would not have to deal with the limited input linear range of a transconductance amplifier. In addition, current-mode circuits are also usually more compact than the voltage-mode counterparts.

VI. Experimental Results from an aVLSI EMD

In these experiments, we measured the output of a single fabricated aVLSI EMD. We used the output current of the EMD to charge or discharge a capacitor on a node V_{mot}, which also has a leak conductance to a reference voltage V_{ref} of 2.5 V. If the input to the chip moves in the preferred direction V_{mot} increases above 2.5 V. If the input moves in the null direction V_{mot} decreases below 2.5 V. The temporal responses of an EMD to a sinewave grating of contrast 0.2 moving in the preferred direction are shown in Fig. 10(a) and in the null direction in Fig. 10(b). The contrast described in the experiment results is the Michelson contrast $(I_{\max} - I_{\min})/(I_{\max} + I_{\min})$, where $I_{\max}$ and $I_{\min}$ are the maximum and minimum intensities respectively of the stimulus. Notice the frequency doubling of the output in these figures.

We plotted the dependence of the aVLSI EMD on the temporal frequency of the input by presenting to the chip a fixed spatial frequency sinewave moving at different velocities. We measured the temporal frequency of the input as seen by the photoreceptor circuit and the average EMD output for each velocity. The results are shown in Fig. 11(a). The upper curve corresponds to the stimulus moving in the preferred direction and and the lower curve is obtained from a stimulus moving in the null direction. The shape of the response is similar to that measured in the HS cell of the fly as shown in Fig. 11(b). This figure was adapted from the work of Hausen [15]. The output of this wide-field cell can be predicted by the EMD model as shown by Egelhaaf and Borst [8]. The range of frequencies for which there is a response extends from about 1 Hz to about 25 Hz.

We also measured the direction selectivity of the output to a square-wave grating moving at different orientations. The response of the chip can be approximated by a cosince function as shown in Fig. 12.

VII. Experimental Results from an aVLSI HS Cell

The figures described in this section are taken from the output of an aVLSI HS cell, which aggregates the outputs of 37 EMDs

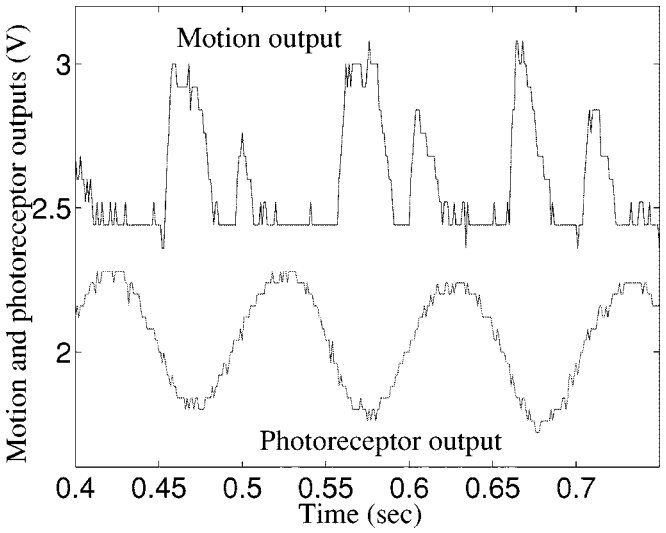

(a)

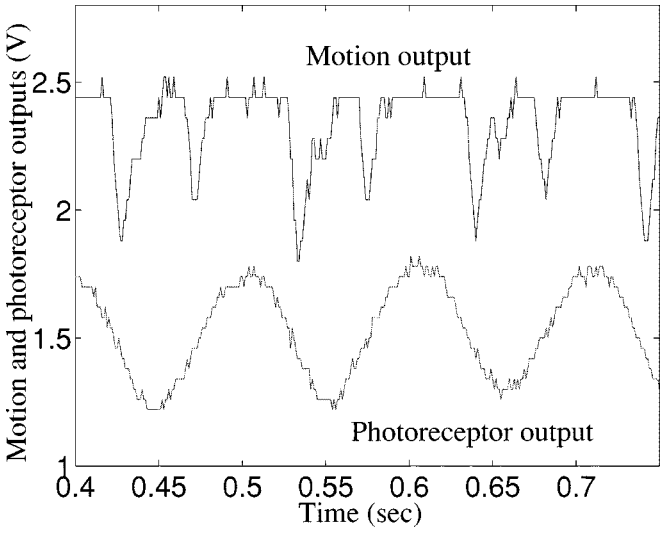

(b)

Fig. 10. Responses of the silicon EMD to a sinewave grating of contrast 0.2 moving at a temporal frequency of 10 Hz. Notice the frequency doubling in output of the EMD. (a) Response of EMD to sinewave moving in the preferred direction. The photoreceptor output has been shifted down by 0.1 V. (b) Output of EMD to the sinewave grating moving in the null direction. The photoreceptor output has been shifted down by 0.6 V.

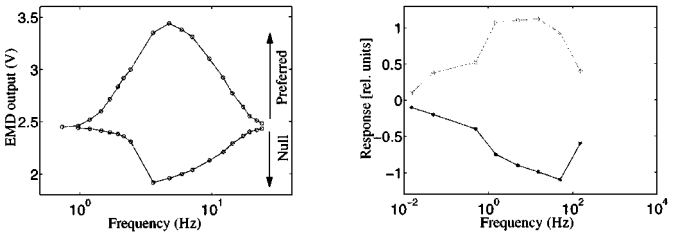

(a) (b)

Fig. 11. Temporal frequency response of silicon EMD and HSE cell. (a) Frequency response of the silicon EMD circuit to a fixed spatial frequency sinewave of contrast 0.92 moving at different velocities. The temporal frequency of the input as seen by the photoreceptor circuit is measured for each velocity. The contrast here is defined as the Michelson contrast, $(I_{\max} - I_{\min})/(I_{\max} + I_{\min})$ The upper curve is obtained for a stimulus moving in the preferred direction and the lower curve is obtained for a stimulus moving in the null direction. (b) Data from HSE cell replotted from Fig. 5(c) in [15]. Again, the upper and lower curves are obtained for stimuli moving in the preferred and null directions, respectively.

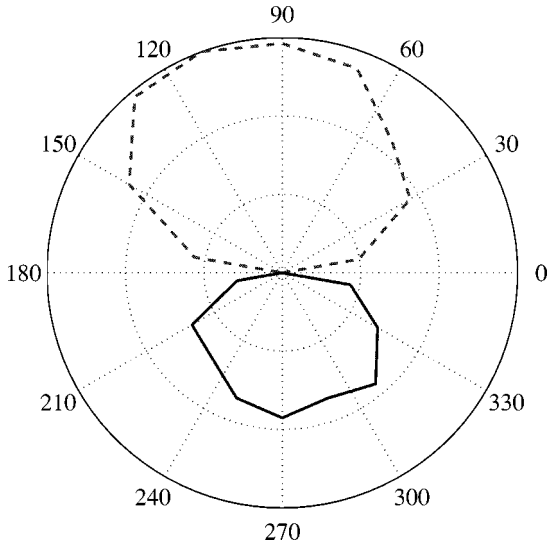

Fig. 12. Response of the silicon EMD to a sinewave grating moving at 10 Hz in the preferred direction (dashed line) and null direction (solid line) at different orientations plotted in polar coordinates. The radius of the plot is 1.608 V and the Michelson contrast of the grating is 0.7. The plot shows the cosine tuning of the EMD response to the stimulus orientation.

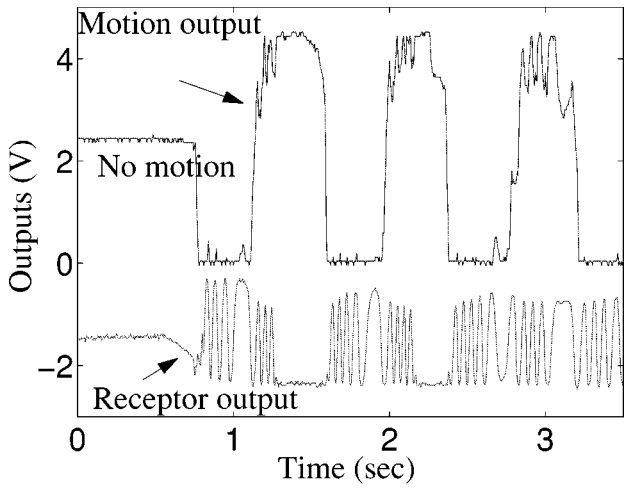

Fig. 13. Global motion output as computed from the linear summation of the outputs from six EMDs in response to a sinewave grating that moves from rest to alternating between moving at a frequency of 2 Hz in the preferred direction and the null direction. The photoreceptor signal has been shifted down by 3 V.

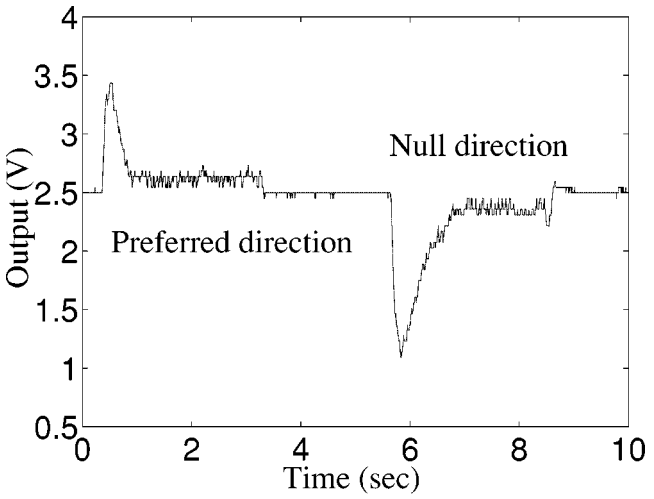

Fig. 14. Transient response of motion output computed from the nonlinear aggregation of 37 EMD outputs in response to a sinewave of contrast 0.58 that starts moving from rest to a frequency of 14 Hz. The large transient response at the start of the motion is not always present at every trial and depends on the output states of the individual blocks in the EMD.

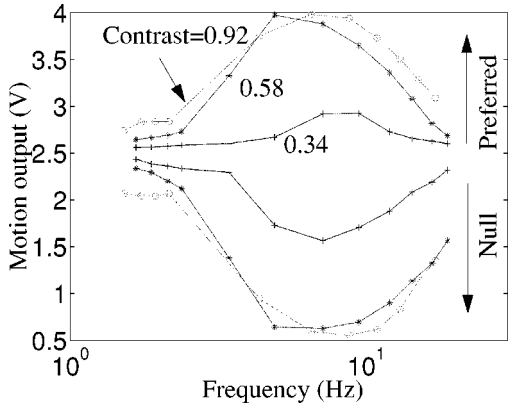

Fig. 15. Frequency response of silicon HS cell with aggregated output from 37 EMDs. The frequency response was measured at three contrasts, 0.34, 0.58, and 0.92. The curves for the contrasts 0.58 and 0.92 almost overlap showing that the motion output was independent of the stimulus contrast for values above 0.58.

using the circuit shown in Fig. 9. For experimental measurements, the outputs of the aggregator circuit I_{aggp} and I_{aggn} are used to charge and discharge a capacitor, respectively, on a node V_{mot}, which also has a leak conductance to a reference voltage V_{ref}. These currents could also be read individually.

A simple summation of the EMDs outputs will lead to an HS output that increases as more EMDs are stimulated. In Fig. 13, we showed the effect of linearly adding the motion outputs of the individual EMDS. The current outputs of the EMDs are used to charge or discharge a capacitor on a common node. The temporal variation in the output is not present but the output saturates at the power rails if enough EMDs are stimulated. Under this condition, it would not be possible to measure the motion quantitatively from the output. Even if we summed the preferred and null output currents of the EMDs to create a global preferred current and a global null current, these global currents increase with the number of stimulated EMDs.

By using nonlinear aggregation of the EMD outputs, we can prevent saturation of the output at the rails. The transient response of the aggregator circuit to an input sinewave grating that starts moving from rest to 14 Hz in the preferred direction and in the null direction is shown in Fig. 14. The large transient response at the start of the motion is not always present over different trials and depends on the output states of the individual blocks of the EMD. These data also show that the steady-state output does not saturate at the rails.

The temporal frequency response of the silicon HS cell was measured for three different contrasts (Fig. 15). The curves for the two higher contrasts, 0.58 and 0.92, almost overlap, thus showing that aggregator output is independent of contrast at least above 0.58. This contrast saturation property is necessary if we do not want the motion output to depend on the signal contrast. Egelhaaf and Borst have shown physiologically that the response of the biological HS cell saturates for contrasts above

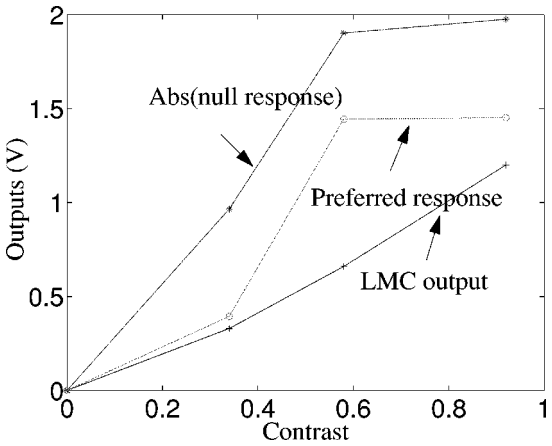

Fig. 16. Plots of the peak preferred and null responses of the silicon HS cell versus contrast. The peak responses are measured for each of the contrast curves in Fig. 15. The responses plotted were subtracted from the resting voltage of 2.5 V. The figure also shows the linear response of the LMC output against contrast; while the motion output saturates for contrasts above approximately 0.45. The same property is observed in biological cells.

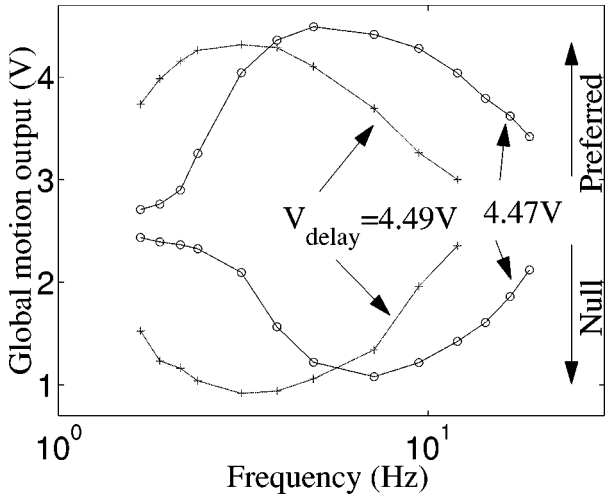

Fig. 17. Frequency response of the HS output for two different time constants of the lowpass filter. The time constant is set by a bias voltage $V_{\rm delay}$. A lower $V_{\rm delay}$ value means a smaller time constant of the filter. The curves show the average response of the circuit to a stimulus moving in the preferred and null directions at two different delay bias settings, i.e., 4.47 and 4.49 V.

0.3–0.4 [8]. This response saturation happens after the LMC circuit as shown in Fig. 16. The LMC output is linearly proportional to the input contrast (Fig. 16) while the preferred and null outputs (measured at the peak response of the curves in Fig. 15) of the aggregator circuit saturate when the contrast exceeds 0.4.

The temporal frequency at which the silicon HS response peaks in Fig. 15 is dependent on the time constant of the low-pass filter τ. We can tune this temporal frequency by changing the bias voltage of the low-pass filter $V_{\rm delay}$ in the system. This shift in the temporal frequency at which the circuit response peaks is shown in Fig. 17 for two different delay settings of 4.47 and 4.49 V.

VIII. Conclusion

The aVLSI motion sensor in this work models the motion computation in the fly visual system. The sensor creates a global motion output from the nonlinear aggregation of 37 elementary motion detectors so that the motion output is independent of stimulus area and contrast. We employed various circuit techniques to generate a robust motion signal by reducing the effects of background intensity and mismatches on the motion computation. This motion sensor differs from some of the other motion circuits, for example, by Sarpeshkar *et al.* [24] and Etienne–Cummings *et al.* [9], as the entire computation up the motion output stage is performed on analog signals. In the implementations mentioned above, a pulse which codes the presence of an "edge" in the scene is first created before the motion of this "edge" is computed. Our circuit implementation differs from Harrison and Koch's implementation in 1998 [12], and includes the contrast normalization circuit, the laminar circuits, and the nonlinear aggregation response of the wide-field cells.

We have used the outputs of these motion sensors as inputs to a controller system on a robot [20]. The system exhibits two behaviors similar to those of the fly; optomotor response and fixation. This system allows us to evaluate models of visuo-motor controllers in working systems. The interaction of these continuous-time sensors with the motor system provides a powerful method of exploring real-time interaction of the robot with its environment.

Acknowledgment

The author would like to thank R. Douglas for supporting this paper, the MOSIS foundation for fabricating this circuit, and A. M. Whatley and T. Delbrück for proofreading and critical reading of this paper's manuscript.

References

[1] A. G. Andreou and K. Strohbehn, "Analog VLSI implementation of the Hassenstein–Reichardt–Poggio models for vision computation," in *Proc. IEEE Int. Conf. on Systems, Man, and Cybernetics*, Nov. 1990, pp. 707–710.

[2] R. Benson and T. Delbrück, "Direction-selective silicon retina that uses null inhibition," in *Advances in Neural Information Processing Systems*, J. Moody, S. Hanson, and R. Lippmann, Eds. San Mateo, CA: Morgan Kaufman, 1992, vol. 4, pp. 756–763.

[3] A. Borst, M. Egelhaaf, and J. Haag, "Mechanisms of dendritic integration underlying gain control in fly motion-sensitive interneurons," *J. Comput. Neurosci.*, vol. 2, pp. 5–18, Mar. 1995.

[4] T. Delbrück, "*Bump* circuits for computing similarity and disimilarity of analog voltages," presented at the Int. Joint Conf. Neural Networks, Seattle, WA, July 1991.

[5] ——, "Silicon retina with correlation-based velocity-tuned pixels," *IEEE Trans. Neural Networks*, vol. 4, pp. 529–541, May 1993.

[6] T. Delbrück and C. A. Mead, "Analog VLSI phototransduction by continuous-time, adaptive, logarithmic photoreceptor circuits," in *CNS Memo 30*. Pasadena, CA: California Inst. Tech., 1994.

[7] C. Diorio, P. Hasler, B. A. Minch, and C. Mead, "Floating-gate MOS synapse transistors," in *Neuromorphic Systems Engineering: Neural Networks in Silicon*, T. S. Lande, Ed. Boston, MA: Kluwer, 1998, pp. 315–338.

[8] M. Egelhaaf and A. Borst, "Transient and steady-state response properties of movement detectors," *J. Opt. Soc. Amer. A*, vol. 6, no. 1, pp. 116–127, 1989.

[9] R. Etienne-Cummings, J. Van der Spiegel, and P. Mueller, "A focal-plane visual-motion measurement sensor," *IEEE Trans. Circuits Syst. I*, vol. 44, no. 1, pp. 55–66, Jan. 1997.

[10] B. Gilbert, "A monolithic 16-channel analog array normalizer," *IEEE J. Solid-State Circuits*, vol. SC-19, pp. 956–963, June 1984.

[11] J. Haag, M. Egelhaaf, and A. Borst, "Dendritic integration of motion information in visual interneurons of the blowfly," *Neurosci. Lett.*, vol. 140, no. 2, pp. 173–176, June 1992.

[12] R. R. Harrison and C. Koch, "An analog VLSI model of the fly elementary motion detector," in *Advances in Neural Information Processing Systems*, M. Jordan, M. Kearns, and S. Solla, Eds. San Mateo, CA: Morgan Kaufman, 1998, vol. 10, pp. 283–284.
[13] ——, "An analog VLSI implementation of a visual interneuron: Enhanced sensory processing through biophysical modeling," *Int. J. Neural Syst.*, vol. 9, no. 5, pp. 391–396, Oct. 1999.
[14] B. Hassenstein and W. Reichardt, "Systemtheoretische analyze der zeit-, reihenfolgen- und vorzeichenauswertung bei der bewegungsperzeption des Rüsselkäfers Chlorophanus," *Z. Naturforsch*, vol. 11b, pp. 513–524, 1956.
[15] K. Hausen, "Motion sensitive interneurons in the optomotor system of the fly. I. The horizontal cells: Structure and signals," *Biol. Cybern.*, vol. 45, pp. 143–156, 1982.
[16] M. Juusola, R. O. Uusitola, and M. Weckström, "Transfer of graded potentials at the photoreceptor-interneuron synapse," *J. Gen. Physiol.*, vol. 105, pp. 115–148, 1995.
[17] J. Kramer, R. Sarpeshkar, and C. Koch, "Pulse-based analog VLSI velocity sensors," *IEEE Trans. Circuits Syst. II*, vol. 44, no. 2, pp. 86–101, Apr. 1997.
[18] S. Laughlin, "Coding efficiency and visual processing," in *Vision: Coding and Efficiency*, C. Blakemore, Ed. Cambridge, U.K., England: Cambridge Univ. Press, 1993, pp. 25–31.
[19] S. C. Liu, "Neuromorphic Models of Visual and Motion Processing in the Fly Visual System," Ph.D. dissertation, Calif. Inst. Tech., Pasadena, CA, 1997.
[20] S. C. Liu and A. Usseglio-Viretta, "Visuo-motor fly-like responses of a robot using a VLSI motion-sensitive chips," in *2nd Int. ICSC Symp. Neural Comput.*, Berlin, Germany, May 2000, pp. 23–26.
[21] A. Moini, A. Bouzerdoum, K. Eshraghian, X. Yakovleff, A. Nguyen, M. A. Blanksby, R. Beare, D. Abbott, and R. Bogner, "An insect vision-based motion detection chip," *IEEE J. Solid-State Circuits*, vol. 32, pp. 279–284, Feb. 1997.
[22] W. Reichardt, T. Poggio, and K. Hausen, "Figure-ground discrimination by relative movement in the visual system of the fly, part II: Toward the neural circuitry," *Biol. Cybern.*, vol. 46, pp. 1–30, 1983.
[23] R. Sarpeshkar, W. Bair, and C. Koch, "An analog VLSI chip for local velocity estimation based on Reichardt's motion algorithm," in *Advances in Neural Information Processing Systems*, S. J. Hanson, J. Cowan, and L. Giles, Eds. San Mateo, CA: Morgan Kaufman, 1993, vol. 5, pp. 781–788.
[24] R. Sarpeshkar, J. Kramer, G. Indiveri, and C. Koch, "Analog VLSI architectures for motion processing: From fundamental limits to system applications," *Proc. IEEE*, vol. 84, pp. 969–987, July 1996.
[25] S. Single and A. Borst, "Dendritic integration and its role in computing image velocity," *Science*, vol. 281, pp. 1848–1850, 1998.

Shih-Chii Liu received the B.S. degree in electrical engineering from Massachusetts Institute of Technology in 1983 and the M.S. degree in electrical engineering from University of California, Los Angeles in 1988. She received the Ph.D. degree in the computation and neural systems program from California Institute of Technology in 1997.

She is currently an Überassistent at the Institute of Neuroinformatics, ETH/UNIZ in Zurich, Switzerland. Her research interests encompass computational neuromorphic models of visual processing in biological systems.